

Supplementary Material: Parameter Studies

The following sections analyse interferometric estimates of source-receiver Green's functions between \mathbf{x}_1 and \mathbf{x}_2 with boundary sources and receivers confined to linear surface arrays, as shown in **Fig. 7**. Each estimate is constructed using only the single term in the integrand of Eq. (8) that is shown in the section title (i.e., the estimate is constructed by ignoring all other terms). Thus we illustrate the contribution and properties of each term individually. The only exception is the first section below which analyses the case where all terms are considered (i.e., where the full Eq. (8) is used).

GGG*: No wavefield separation

The solid line in **Fig. C-1** shows the interferometric estimate using all of Eq. (8), with the boundaries S and S' constrained to the surface as in **Fig. 7**. Both the causal and acausal wave between \mathbf{x}_1 and \mathbf{x}_2 appear to be constructed; however, we show in **Appendix B** that what looks like the causal scattered wave is in fact a pseudo-physical arrival. The direct wave is missing since stationary points \mathbf{a} and \mathbf{b} are not sampled in this geometry. Instead a number of non-physical events occur that are not predicted by the directly modelled Green's function (dashed line). These events can be stationary or non-stationary and occur due to the lack of boundary sources and receivers in the subsurface. The origin of the different types of non-physical arrivals will be investigated in detail by the following numerical examples. Some non-physical events can be suppressed by tapering the contributions from the end points of the boundaries (**Fig. C-1b**). **Fig. C-1c** displays the interferometric estimate using both monopole and dipole sources (i.e., using Eq. (1) and (2) instead of the approximate Eq. (3) and (4)). This reduces the amplitudes of non-physical arrivals (e.g. at 0.25 s) relative to the amplitudes of physical arrivals. Using a sparser source and receiver coverage along the boundaries evokes additional non-physical events (e.g., at 0.5 s, **Fig. C-1d**). As the following examples will show, each of these events can be attributed to particular terms of Eq. (8).

$G_0G_0G_S^*$

Table 1 shows that the term $G_0G_0G_S^*$ accounts for the construction of four events related to different stationary pairs. In the geometry used (**Fig. C-2**), however, only the stationary points **c** and **e** are spanned by sources and receivers, hence only the acausal scattered wave is constructed (**Fig. C-3**). Besides this physical arrival, non-physical events are observed at approx. (1) -0.05 s, (2) -0.15 s, and (3) -0.25 s. Events (2) and (3) originate from the end points of the receiver boundary where the contributions of non-stationary boundary points are not cancelled due to the abrupt truncation of the summation—see **Fig. 10b**. Similarly, event (1) originates from the end points of the source boundary: **Fig. 10a** shows that it is generated in the first step and then contributes to the second step. All such non-physical arrivals can be significantly suppressed by a spatial taper (**Fig. C-3b**). Moreover, the non-physical events are non-stationary and will vary in travel time when, for example, the lengths of the boundaries are changed. Therefore they can easily be discriminated from the stationary scattered wave arrival. Using dipole sources enhances the ratio of physical to non-physical energy (**Fig. C-3c**). Increasing the inter-source and inter-receiver distance along the boundaries still retrieves a good estimate of the acausal scattered wave (**Fig. C-3d**). In the presented example the decimation of the boundary points by up to a factor of six did not create additional non-physical events, but this depends on the slope of the travel time curve in the correlation gather (Mehta *et al.* 2008) (also compare **Fig. 13c** and **14c**).

$G_SG_SG_S^*$

Stationary phase analysis predicts that the term $G_SG_SG_S^*$ constructs an event with the same travel time as the causal scattered wave, and that any source-receiver pair is stationary and contributes energy to the constructed arrival (**Table 1**). This is confirmed in the numerical examples (**Fig. C-5**): a single event appears on the trace where the causal wave is expected, and unlike in other terms, no spurious events associated with the boundaries' end points are observed regardless of the parameter

constellation. This can be understood in terms of the correlation gathers (**Fig. 10c** and **d**): in inter-receiver interferometry as well as inter-source interferometry the travel time curve in the correlation gather is a constant, i.e., the travel time of each individual event constructed from a single source or receiver, respectively, is independent of the source or receiver position along the boundaries. The stationary points are actually stationary planes, and all events sum up constructively to give a single arrival. However, the constructed event is not the causal scattered wave but in fact a non-physical event that arrives at the same travel time, as we discuss in detail in **Appendix B**. Moreover, we show that in 2D it matches also the waveform of the physical arrival, and that its amplitude differs by a factor proportional to the imaginary part of the scattering matrix. Hence, the *pseudo*-physical event constructed from $G_S G_S G_S^*$ gives a good estimate of the causal scattered wave even when using only a partial integration boundary. In fact, a single source-receiver pair on the surface is sufficient to construct the pseudo-physical wave, and varying the parameters does not affect the quality of the constructed wave, nor does it introduce spurious energy (compare **Figs C-5a** to **d**).

$G_0 G_S G_S^*$

The receiver array in the geometry used (**Fig. 7**) samples the stationary point $\mathbf{x}' = \underline{\mathbf{e}}$ (**Fig. 3**), which for the term $G_0 G_S G_S^*$ combined with any source on S provides a stationary non-physical arrival at approx. -0.05 s (**Table 1**, **Fig. C-8**). The second event around 0.2 s is *non*-stationary and non-physical as it originates from the abrupt truncation of the summation over receivers. **Fig. C-7** shows that only the acausal event is stationary under changing boundary conditions. Although this stationary event is termed non-physical its travel time has a useful physical interpretation: while the travel time of a (physical) scattered wave between \mathbf{x}_1 and \mathbf{x}_2 (e.g. from term $G_0 G_0 G_S^*$) is given by the *sum* of the travel times from \mathbf{x}_1 to \mathbf{x}_S and from \mathbf{x}_S to \mathbf{x}_2 , the travel time of the non-physical event corresponds to the *difference* of the travel times from \mathbf{x}_S to \mathbf{x}_2 and from \mathbf{x}_1 to \mathbf{x}_S . The combination of both, the sum and the difference, can be solved for the travel times of each part (from \mathbf{x}_1 to \mathbf{x}_S and from \mathbf{x}_S to \mathbf{x}_2 ,

respectively) and uniquely defines the location of a scatterer located below \mathbf{x}_1 and \mathbf{x}_2 .

$G_S G_0 G_S^*$

The term $G_S G_0 G_S^*$ can be interpreted analogously to term $G_0 G_S G_S^*$: only the stationary points that account for the construction of the non-physical event ($\forall \mathbf{x}', \mathbf{x} = \underline{\mathbf{c}}$, **Fig. 3**) are spanned by the source and receiver arrays and provide a stationary event at approx. 0.05 s (**Table 1, Fig. C-10**). The travel time of this event corresponds to the difference between the travel times from \mathbf{x}_1 to \mathbf{x}_S and from \mathbf{x}_S to \mathbf{x}_2 . The second event at approx. 0.15 s is also non-physical but is non-stationary as it is an artefact from the abrupt truncation of the source boundary (see correlation gather in **Fig. 10g**). Its travel time therefore changes with varying aperture of the source array, which makes it distinguishable from the stationary event (see also **Fig. C-7**), and its amplitude can be reduced by tapering on the boundary (**Fig. C-10b**) and by using dipole sources (**Fig. C-10c**). Decimating the source and receiver boundary by a factor of three does not introduce additional non-physical energy (**Fig. C-10d**).

$G_0 G_0 G_0^*$

Because the stationary points associated with $G_0 G_0 G_0^*$ (**a** and **b** in **Fig. 3**) are not spanned by the surface boundaries the signal that is constructed (**Fig. C-13**) does not match the direct wave but consists of (at least two) non-physical arrivals. As can be seen in **Fig. C-12** these events are not stationary but move out with increasing depth \mathbf{d}_2 in **Fig. C-11**. For smaller depths the event converges towards the true direct arrivals at 0.15 s and -0.15 s, respectively, whereas for larger depths an asymmetric move out towards positive travel times is observed. The cross-correlation gather (**Fig. 10j**) reveals that the non-physical energy originates from the contribution of non-stationary points at the edges of the boundaries. The events' amplitudes are significantly reduced by tapering the end point sources and receivers (**Fig. C-13b**), and are further reduced by including dipole sources (**Fig. C-13c**). Increasing the inter-source and inter-receiver spacing along the boundaries S and S' , respectively, introduces further spurious events on the causal side (**Fig. C-13d**), which occur due to

the incomplete cancellation of non-stationary events in the inter-receiver step when the spacing on boundary S is too large (compare **Figs 12a** and **c**).

$G_S G_S G_0^*$

Meles & Curtis (2013) showed that for the term $G_S G_S G_0^*$ any pair of a boundary source \mathbf{x} and a boundary receiver \mathbf{x}' connected by a straight line passing through the scatterer is stationary and provides a stationary arrival at the travel time of the causal scattered wave (**Table 1**). This configuration cannot, however, be realised when using surface boundaries only: both \mathbf{x} and \mathbf{x}' are always located on the same side of, namely above, the scatter. Therefore no stationary event is constructed, and as before the incomplete boundaries generate non-physical arrivals due to incomplete destructive interference of non-stationary events (**Fig. C-15a**). Applying a taper (**Fig. C-15b**) and using dipole sources (**Fig. C-15c**) suppresses the amplitude of the signal almost completely. A sparse source and receiver coverage along the boundaries (**Fig. C-15d**) generates further spurious events; however, they are not observed in the given time window.

$G_0 G_S G_0^*$

As before, the linear source and receiver arrays do not span the stationary points required to create the events associated with the term $G_0 G_S G_0^*$ (**Table 1**); instead non-physical arrivals occur due to the incomplete cancellation of non-stationary signals. This can be proved following previous arguments by looking at the cross-correlation gathers and the behaviour of the constructed signals under varying source/receiver boundary conditions. The traces in **Fig. C-17** show the effect of different parameter constellations. Most noticeable is the strong amplitude reduction by down weighting the contribution of end point sources and receivers with a taper (**Fig. C-17b**), and the additional reduction by using dipole sources (**Fig. C-17c**). Increasing the inter-source and inter-receiver distance on boundaries S and S' , respectively, produces new spurious events, which, however, lie outside the considered time window (**Fig. C-17d**).

$G_S G_0 G_0^*$

The stationary points for $G_S G_0 G_0^*$ are **c** and **d** in **Fig. 3**, which account for the construction of the causal scattered wave and a non-physical, but stationary event (**Table 1**). Using surface boundaries only, point **d** is not spanned and the expected signals are not constructed. The arrivals shown in **Fig. C-19** are non-physical and non-stationary and originate from incomplete cancellations in the summation of non-stationary events. As before, this can be shown from the cross-correlation gathers. The amplitude can noticeably be reduced by applying a spatial taper (**Fig. C-19b**) and by using dipole sources (**Fig. C-19c**). A coarser source and receiver coverage along the boundaries introduces new spurious arrivals at large travel times (**Fig. C-19d**). See previous sections for a detailed analysis of the generation of non-stationary events.

Figures

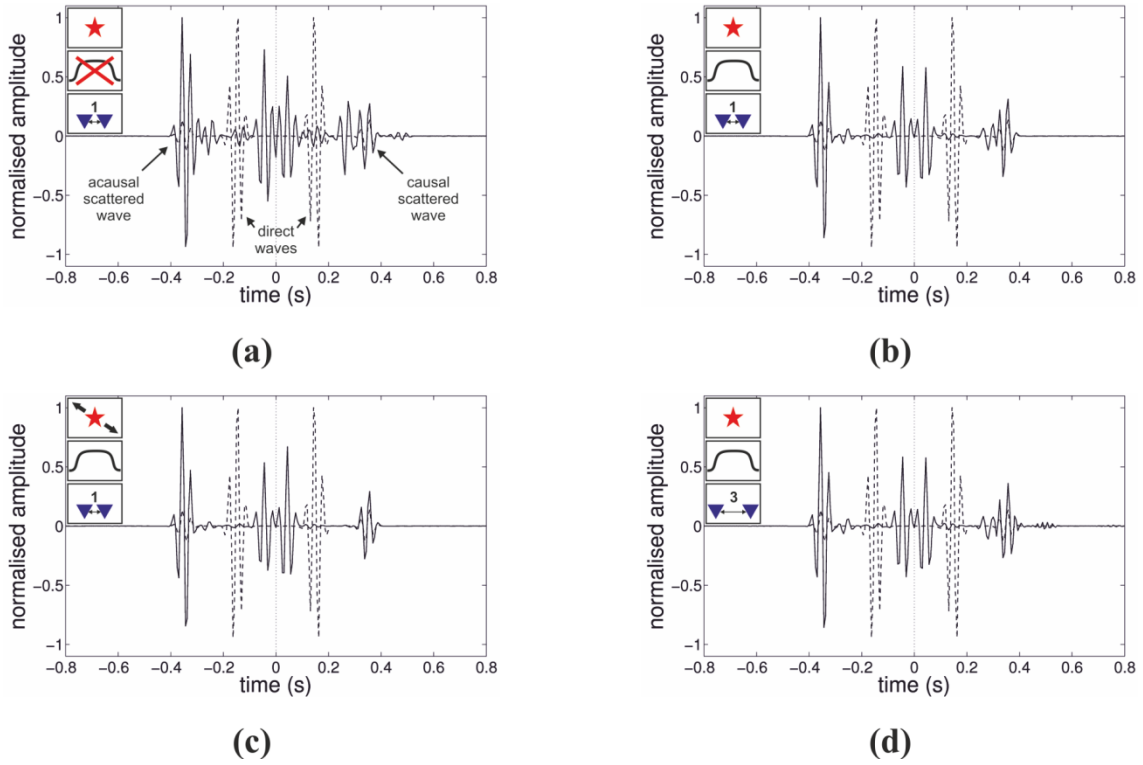


Fig. C-1: Interferometric result of the full integral GGG^* of Eq. (8) (solid line) compared to the true Green's function between \mathbf{x}_1 and \mathbf{x}_2 (dashed line) for different parameter constellations (see **Table 2**). Maximum Amplitudes have been normalised to one.

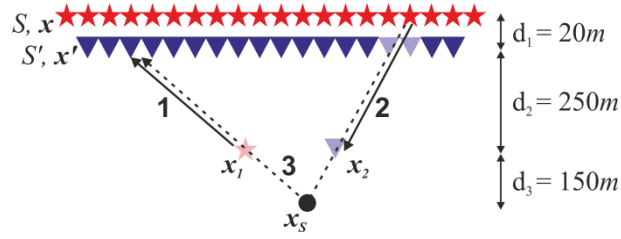


Fig. C-2: Example set of raypaths used in $G_0 G_0 G_S^*$, symbol key as in **Fig. 2**. The dashed line represents the ray of the complex conjugated term. Faded symbols are used to make raypaths visible. Rays shown are 1: $G_0(\mathbf{x}', \mathbf{x}_1)$, 2: $G_0(\mathbf{x}_2, \mathbf{x})$, 3: $G_S^*(\mathbf{x}', \mathbf{x})$.

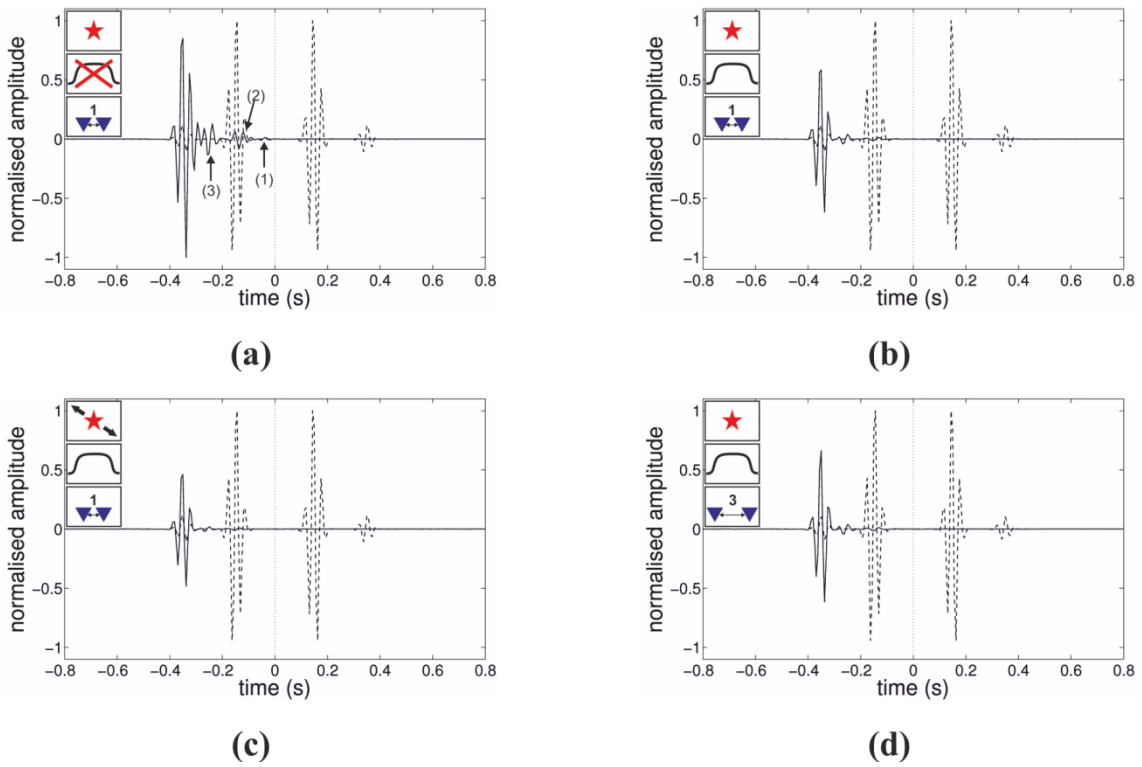


Fig. C-3: Interferometric result of the cross term $G_0 G_0 G_S^*$ in Eq. (8) (solid line) compared to the true Green's function between \mathbf{x}_1 and \mathbf{x}_2 (dashed line) for different parameter constellations (see **Table 2**). Traces have amplitudes that are normalised relative to case (a). Number labels are referred to in the text.

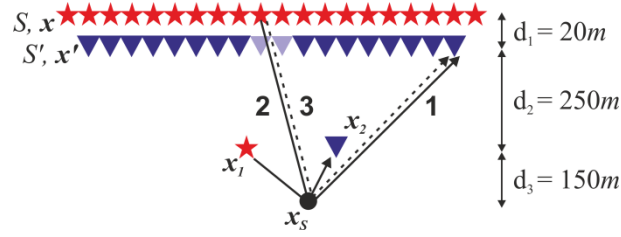


Fig. C-4: Example set of raypaths used in $G_S G_S G_S^*$, symbol key as in **Fig. C-2**. Rays shown are 1: $G_S(\mathbf{x}', \mathbf{x}_1)$, 2: $G_S(\mathbf{x}_2, \mathbf{x})$, 3: $G_S^*(\mathbf{x}', \mathbf{x})$.

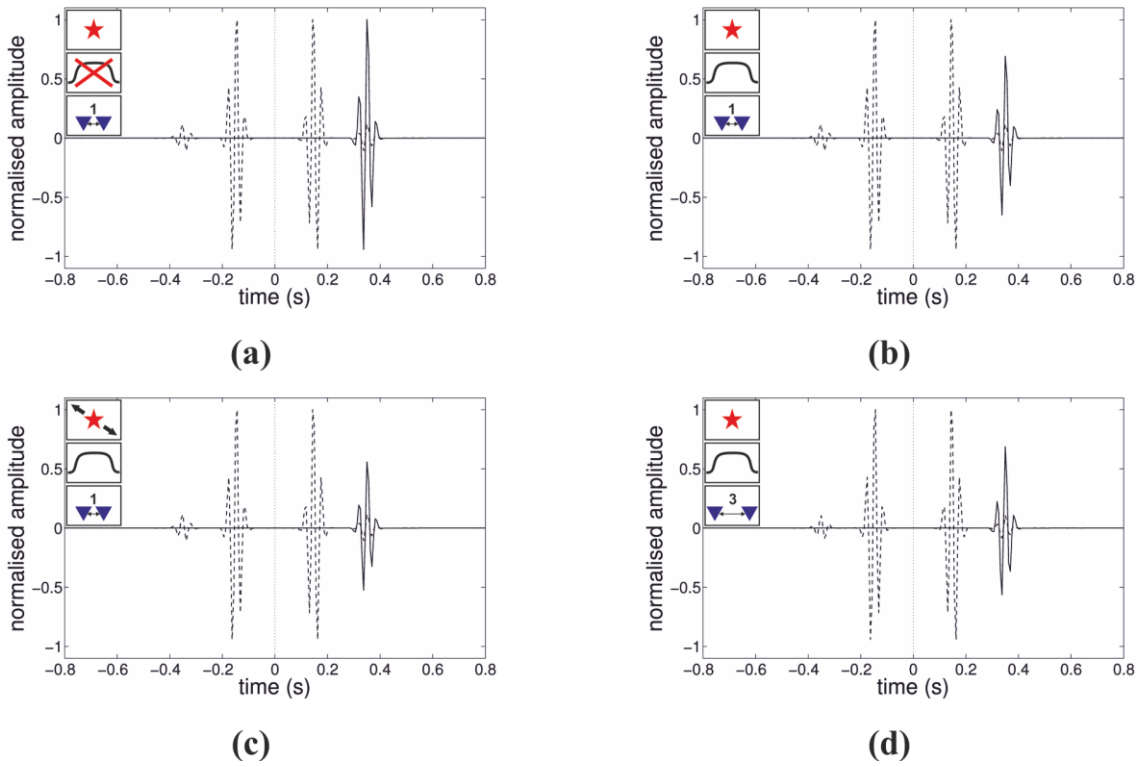


Fig. C-5: Interferometric result of the cross term $G_S G_S G_S^*$ in Eq. (8) (solid line) compared to the true Green's function between \mathbf{x}_1 and \mathbf{x}_2 (dashed line) for different parameter constellations (see **Table 2**). Traces have amplitudes that are normalised relative to case (a).

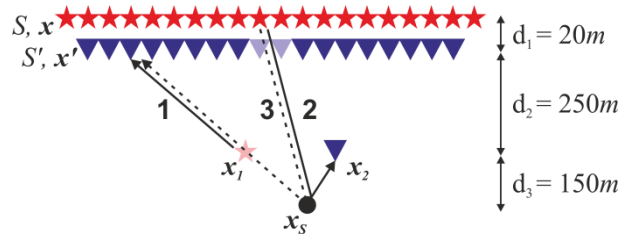


Fig. C-6: Example set of raypaths used in $G_0 G_S G_S^*$, symbol key as in **Fig. C-2**. Rays shown are 1: $G_0(\mathbf{x}', \mathbf{x}_1)$, 2: $G_S(\mathbf{x}_2, \mathbf{x})$, 3: $G_S^*(\mathbf{x}', \mathbf{x})$.

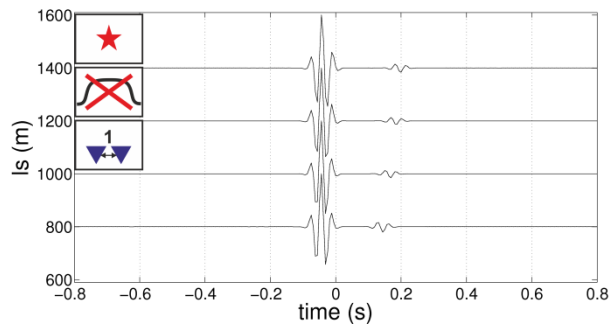
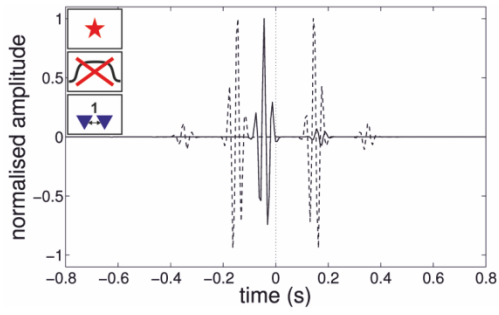
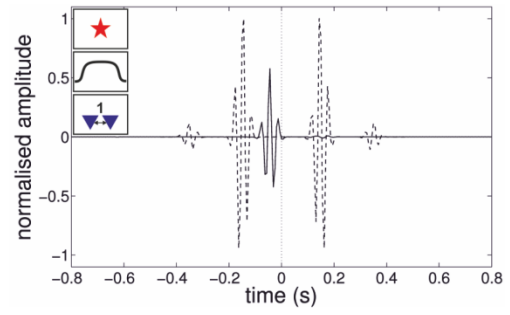


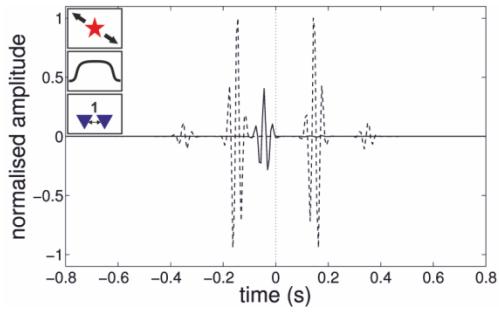
Fig. C-7: $G_0 G_S G_S^*$ for different apertures (length l_s) of both source (l_s) and receiver ($l_s - 100$) boundary showing a stationary (-0.05 s) and a non-stationary (between 0.1 and 0.2 s) non-physical arrival.



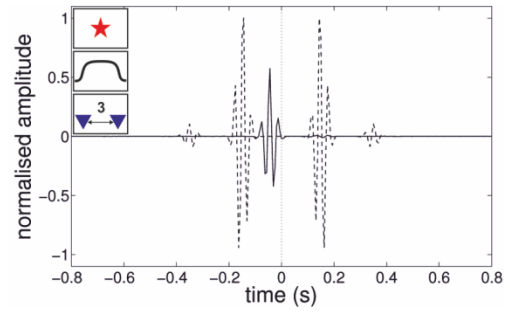
(a)



(b)



(c)



(d)

Fig. C-8: Interferometric result of the cross term $G_0 G_S G_S^*$ in Eq. (8) (solid line) compared to the true Green's function between \mathbf{x}_1 and \mathbf{x}_2 (dashed line) for different parameter constellations (see **Table 2**). Traces have amplitudes that are normalised relative to case (a).

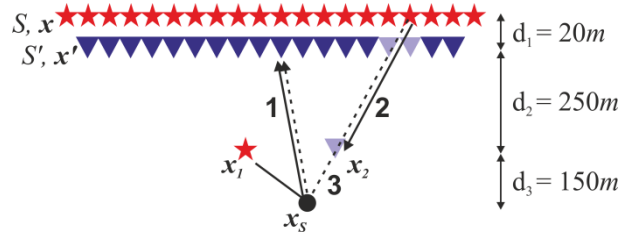


Fig. C-9: Example set of raypaths used in $G_S G_0 G_S^*$, symbol key as in **Fig. C-2**. Rays shown are 1: $G_S(\mathbf{x}', \mathbf{x}_1)$, 2: $G_0(\mathbf{x}_2, \mathbf{x})$, 3: $G_S^*(\mathbf{x}', \mathbf{x})$.

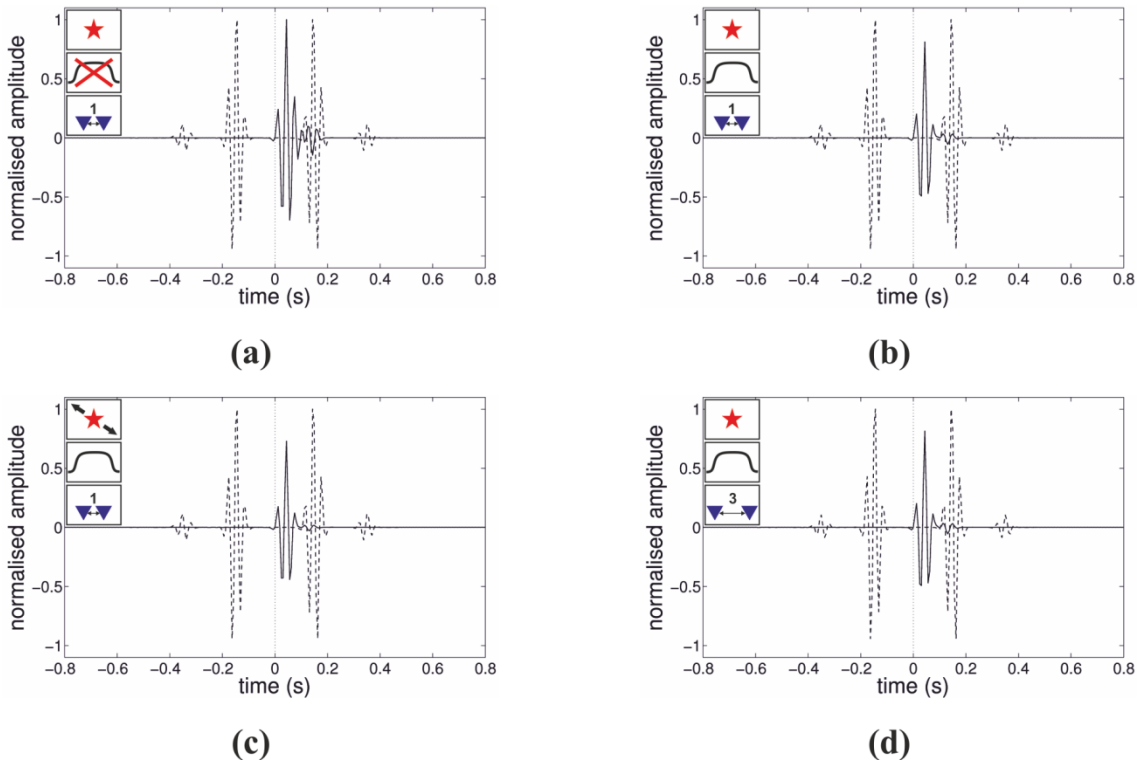


Fig. C-10: Interferometric result of the cross term $G_S G_0 G_S^*$ in Eq. (8) (solid line) compared to the true Green's function between \mathbf{x}_1 and \mathbf{x}_2 (dashed line) for different parameter constellations (see **Table 2**). Traces have amplitudes that are normalised relative to case (a).

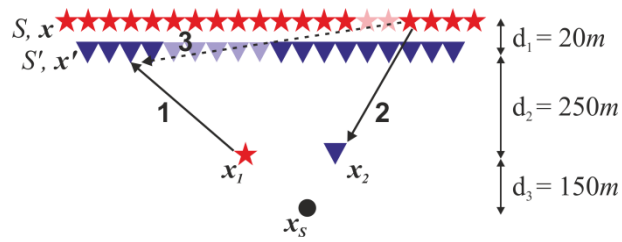


Fig. C-11: Example set of raypaths used in $G_0 G_0 G_0^*$, symbol key as in **Fig. C-2**. Rays shown are 1: $G_0(\mathbf{x}', \mathbf{x}_1)$, 2: $G_0(\mathbf{x}_2, \mathbf{x})$, 3: $G_0^*(\mathbf{x}', \mathbf{x})$.

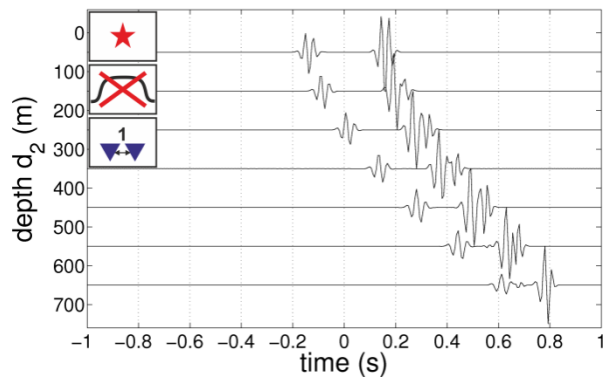
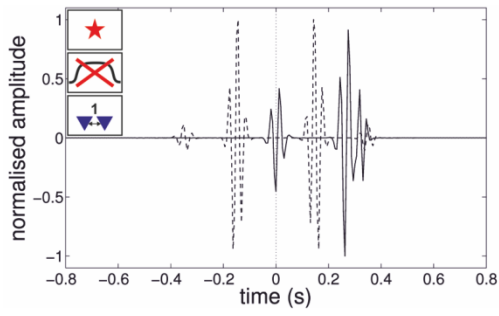
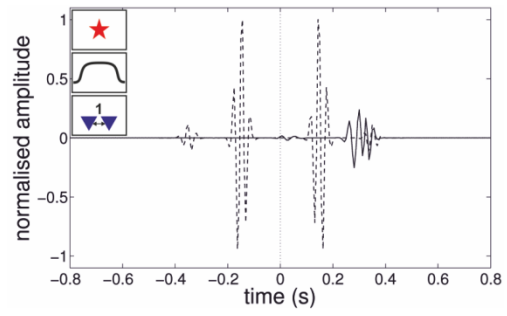


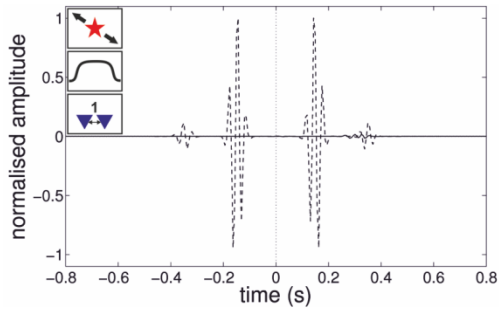
Fig. C-12: $G_0 G_0 G_0^*$ for different depths \mathbf{d}_2 showing the move-out of non-stationary events.



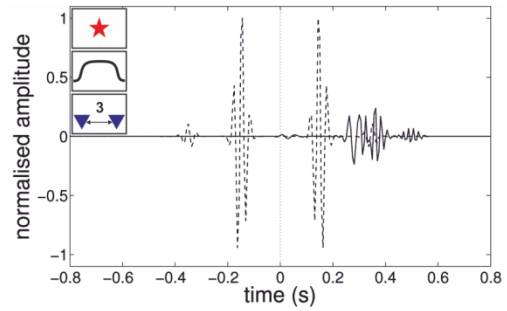
(a)



(b)



(c)



(d)

Fig. C-13: Interferometric result of the cross term $G_0 G_0 G_0^*$ in Eq. (8) (solid line) compared to the true Green's function between \mathbf{x}_1 and \mathbf{x}_2 (dashed line) for different parameter constellations (see **Table 2**). Traces have amplitudes that are normalised relative to case (a).

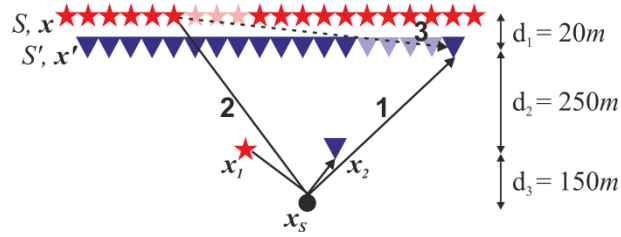


Fig. C-14: Example set of raypaths used in $G_S G_S G_0^*$, symbol key as in **Fig. C-2**. Rays shown are 1: $G_S(\mathbf{x}', \mathbf{x}_1)$, 2: $G_S(\mathbf{x}_2, \mathbf{x})$, 3: $G_0^*(\mathbf{x}', \mathbf{x})$.

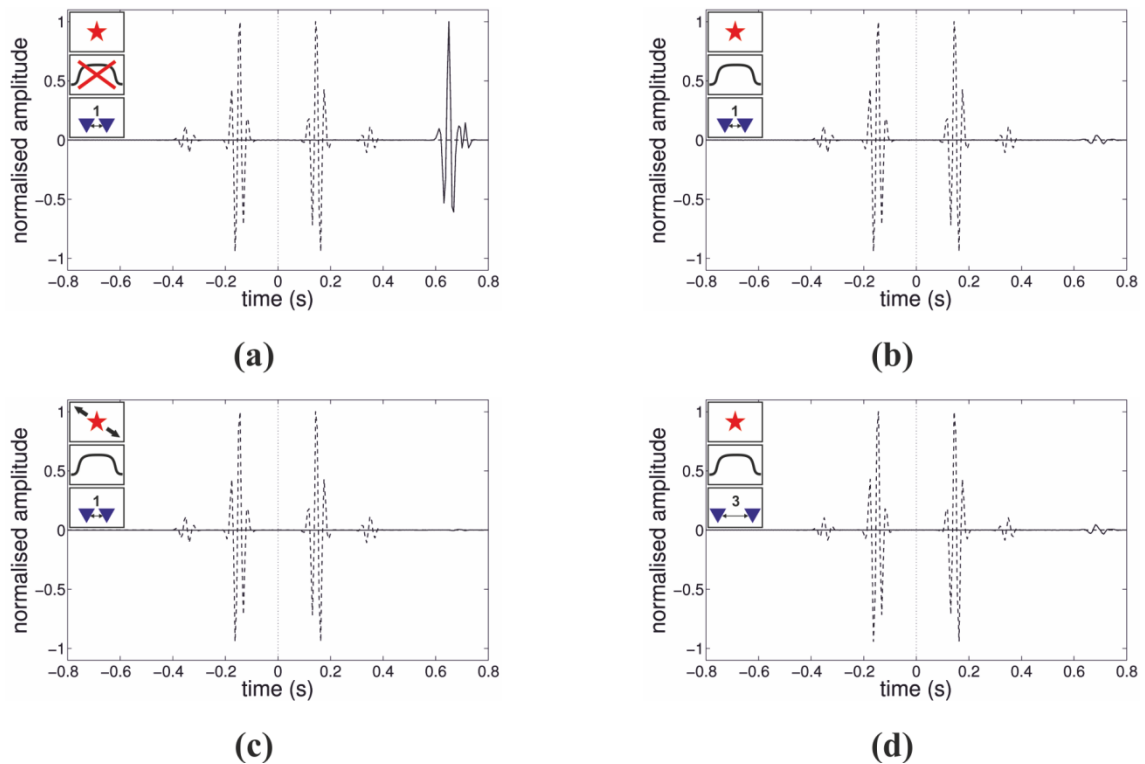


Fig. C-15: Interferometric result of the cross term $G_S G_S G_0^*$ in Eq. (8) (solid line) compared to the true Green's function between \mathbf{x}_1 and \mathbf{x}_2 (dashed line) for different parameter constellations (see **Table 2**). Traces have amplitudes that are normalised relative to case (a).

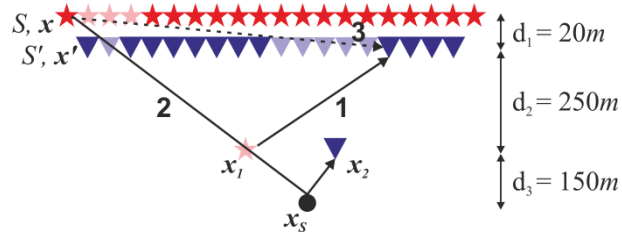


Fig. C-16: Example set of raypaths used in $G_0 G_S G_0^*$, symbol key as in **Fig. C-2**. Rays shown are 1: $G_0(\mathbf{x}', \mathbf{x}_1)$, 2: $G_S(\mathbf{x}_2, \mathbf{x})$, 3: $G_0^*(\mathbf{x}', \mathbf{x})$.

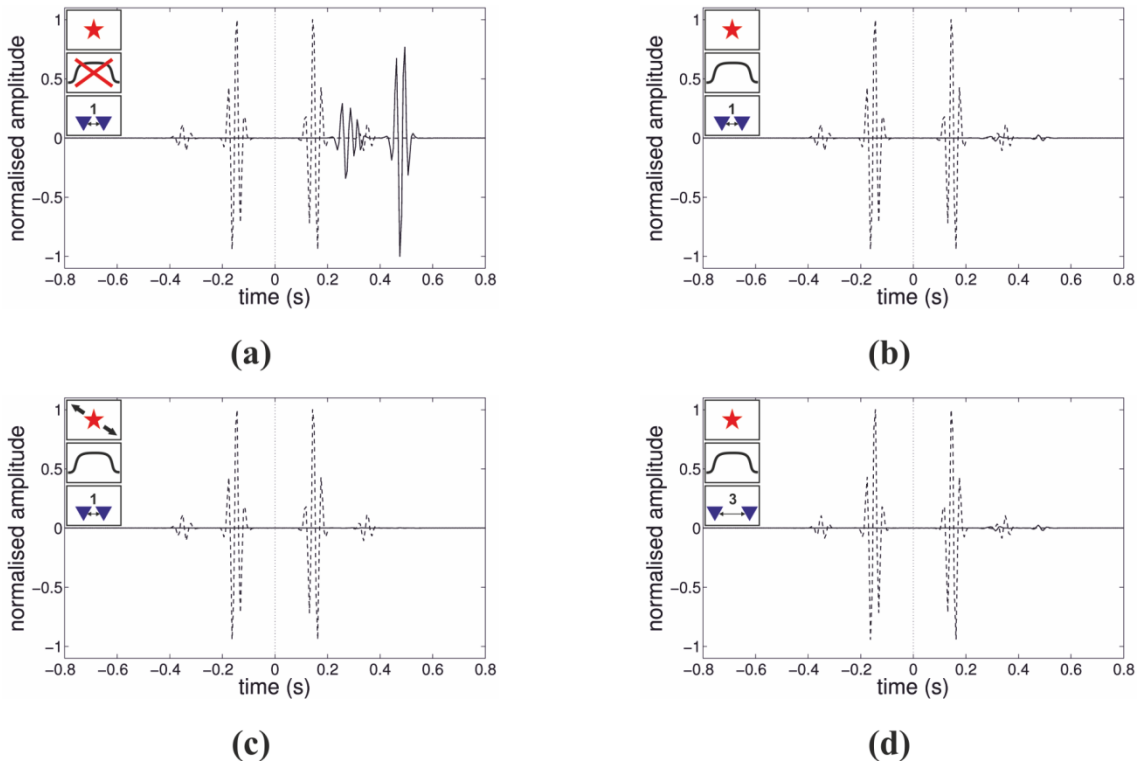


Fig. C-17: Interferometric result of the cross term $G_0 G_S G_0^*$ in Eq. (8) (solid line) compared to the true Green's function between \mathbf{x}_1 and \mathbf{x}_2 (dashed line) for different parameter constellations (see **Table 2**). Traces have amplitudes that are normalised relative to case (a).

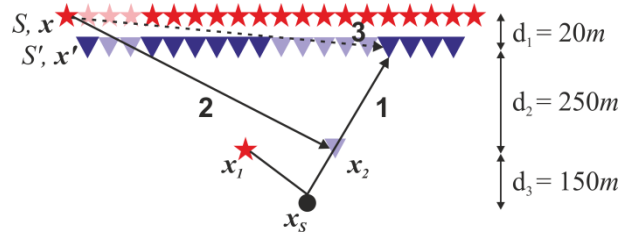


Fig. C-18: Example set of raypaths used in $G_S G_0 G_0^*$, symbol key as in **Fig. C-2**. Rays shown are 1: $G_S(\mathbf{x}', \mathbf{x}_1)$, 2: $G_0(\mathbf{x}_2, \mathbf{x})$, 3: $G_0^*(\mathbf{x}', \mathbf{x})$.

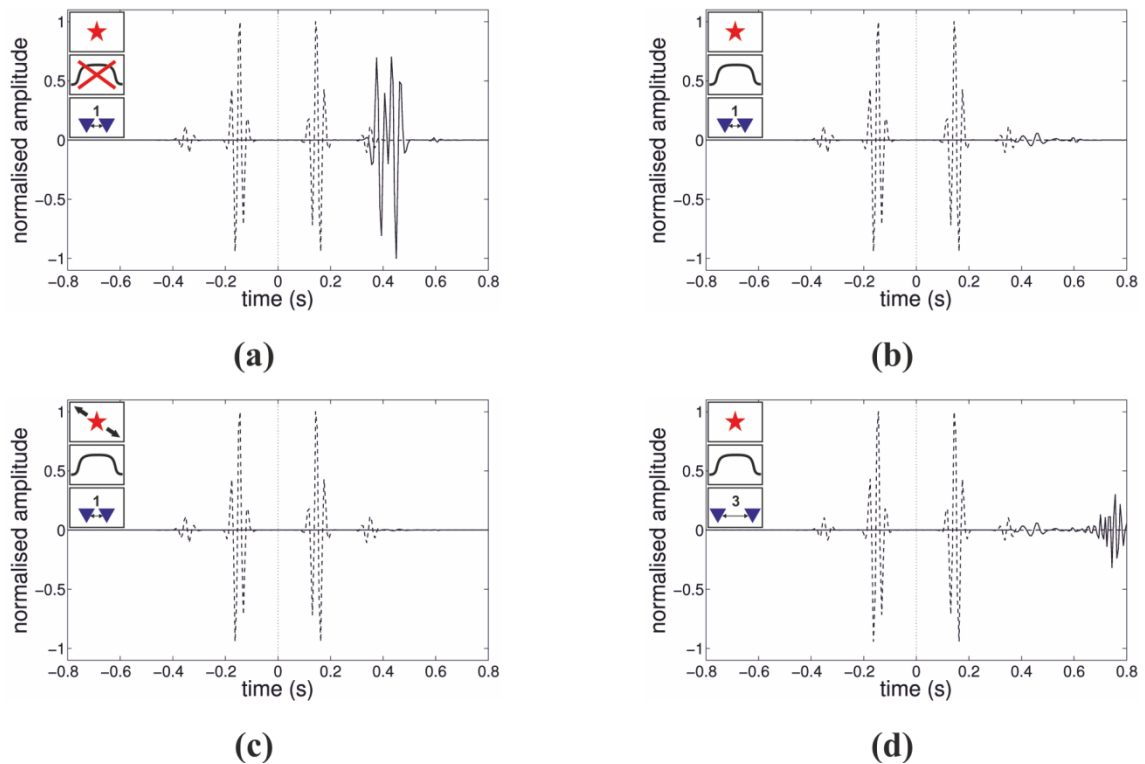


Fig. C-19: Interferometric result of the cross term $G_S G_0 G_0^*$ in Eq. (8) (solid line) compared to the true Green's function between \mathbf{x}_1 and \mathbf{x}_2 (dashed line) for different parameter constellations (see **Table 2**). Traces have amplitudes that are normalised relative to case (a). Inset in (d) shows detail.